# VitalFR3: Wireless Vital Sign Sensing in the Upper Mid-Band (FR3)

Gholamreza Bakhshi and Hatem Abou-Zeid
*Dept. of Electrical and Software Engineering, WAVES LAB, University of Calgary, Canada*
{gholamreza.bakhshi, hatem.abouzeid }@ucalgary.ca

***Abstract*—Frequency range 3 (FR3) is being explored for sixth-generation (6G) integrated sensing and communication (ISAC). However, experimental evidence on the feasibility of physiological sensing in this band is limited. This paper presents VitalFR3, an SDR-based frequency-modulated continuous-wave (FMCW) measurement platform that integrates a direct-sampling Ettus USRP X440 with a SignalCraft SC2470 frequency converter. To the best of our knowledge, this is the first calibrated SDR-based FMCW platform evaluated for respiration and cardiac-rate estimation from human measurements across multiple FR3 center frequencies. Using a $100$ MHz waveform, we operate the platform at six RF center frequencies from $10$ to $22.5$ GHz. We demonstrate how to characterize and calibrate the complete VitalFR3 transmit and receive path directly from loopback recordings, achieving a magnitude error below $0.061$ dB at all six frequencies. We then propose a low-complexity end-to-end processing pipeline for vital sign estimation. This involves the identification of a persistent target-associated response in fast time, respiratory tracking in slow time, followed by cardiac-rate estimation. The system is evaluated across 16 human measurements, achieving a respiratory-rate mean absolute error of $0.758$ breaths per minute, and the majority of the cardiac-rate estimates fall within $\pm 5$ BPM of their reference rates. In a separate breath-hold measurement, the estimated cardiac rate is $84.3$ BPM versus approximately $84.5$ BPM from the reference. These results establish VitalFR3 as a calibrated and configurable measurement platform for experimental physiological sensing across FR3.**

***Index Terms*—Vital sign sensing, FR3, software-defined radio (SDR), frequency-modulated continuous-wave (FMCW), calibration.**

## I. Introduction

Sixth-generation (6G) wireless systems are expected to integrate communication and sensing through Integrated Sensing and Communication (ISAC), enabling shared radio resources to support both data transmission and environmental sensing [1]–[3]. Contactless vital sign sensing is one potential application, since radio signals can capture the small body-surface motions caused by respiration and cardiac activity without requiring wearable sensors [4]. Frequency range 3 (FR3), spanning 7.125–24.25 GHz, lies between sub-6 GHz and millimeter-wave (mmWave) bands, and offers a distinct combination of propagation characteristics, available bandwidth, and phase sensitivity to the small displacements associated with vital signs. While these properties create opportunities for physiological sensing, there are also unique propagation challenges associated with the FR3 band.

Indoor FR3 channels can exhibit rich multipath and considerable delay spread, with waveguide-like propagation reported in some indoor environments [5]. These conditions matter for vital sign sensing because the small phase variations caused by respiration and cardiac motion must be measured in the presence of multiple propagation paths. Most experimental FR3 studies have so far focused on propagation measurements, channel characterization, communication testbeds, and macroscopic sensing tasks [2], [6]–[9]. However, experimental studies of respiration and cardiac sensing in this band remain limited. This leaves an open question of how a programmable FR3 measurement system can be built and utilized for physiological sensing.

Physiological sensing in FR3 requires a measurement platform that can generate and acquire a controlled waveform while preserving the small phase variations associated with respiration and cardiac motion. Compared with more established mmWave sensing bands, FR3 has a less mature ecosystem of integrated sensing instrumentation. Experimental work in this band therefore requires not only sensing methods, but also the development and characterization of the measurement platform itself. To meet this need, we develop VitalFR3, a programmable FR3 measurement platform that combines an Ettus USRP X440 software-defined radio (SDR) with a SignalCraft SC2470 frequency up/down converter. The X440 direct sampling architecture provides control of waveform generation, sampling, and acquisition, while the SC2470 provides frequency translation between the X440 intermediate frequency (IF) and the selected FR3 RF center frequency. The VitalFR3 architecture supports instantaneous bandwidths up to $1.6$ GHz, enabled by the wideband capabilities of the X440 and SC2470.

While the X440 enables IF phase coherence and large bandwidths, it also introduces two instrumentation challenges. First, vital sign sensing requires stable phase measurements together with direct control of the transmitted waveform, sampling, and acquisition timing. The X440 uses a direct-sampling architecture in which the balun-coupled front ends are connected directly to the data converters [10], which means that it does not use internal analog mixers or local oscillators for frequency conversion, nor analog filtering in the analog signal path. Therefore, the converter rate, sampling rate, and placement of the transmitted waveform within the appropriate Nyquist zone must be explicitly controlled. Sec-

This work was supported by infrastructure funded by the Canada Foundation for Innovation (CFI) John R. Evans Leaders Fund (JELF) and the Government of Alberta, Research Capacity Program (RCP).

ond, stable phase measurements from the X440 alone do not characterize the complete sensing path. The SC2470 and fixed components also affect the amplitude, phase, and timing of the recorded signal - hence the complete transmit and receive path must be characterized to establish a consistent measurement reference.

Beyond these instrumentation challenges, physiological recovery and validation introduce further requirements. Calibrated FR3 measurements do not directly provide physiological information. In indoor FR3 environments, rich multipath and delay dispersion can complicate target localization and the recovery of the small phase variations associated with respiration and cardiac motion. An advanced signal processing pipeline is therefore needed to convert the calibrated complex I/Q measurements into physiological estimates. Cardiac sensing also faces a challenging ambiguity when respiratory harmonics enter the cardiac frequency range. In this case, frequency alone may not be sufficient to distinguish the physiological origin of the observed component.

To the best of our knowledge, this paper is the first experimental study to develop and evaluate an SDR-based FR3 platform for contactless respiration and heart-rate estimation across multiple FR3 center frequencies. The main contributions of this work are summarized as follows:

- **Programmable FR3 Measurement Platform:** We introduce VitalFR3, a programmable FR3 measurement platform established by integrating the X440 direct-sampling SDR with the SC2470 FR3 frequency converter. We describe the acquisition configuration needed to correctly control the converter rate, sampling rate, waveform placement, and timing in this architecture. The experimental configuration uses a 100-MHz FMCW waveform at six RF center frequencies between 10 and 22.5 GHz under a fixed acquisition plan. This platform is scalable to substantially wider bandwidths and provides a basis for examining physiological measurements and other FR3 sensing use-cases using direct sampling.
- **End-to-End Calibration of the Platform:** We demonstrate how to characterize and calibrate the complete VitalFR3 transmit and receive path directly from loopback recordings. This involves deriving the required corrections and timing reference for each RF center frequency. Across all six RF center frequencies, our calibration procedure reduces the remaining magnitude error to below $0.061$ dB and establishes the measurement reference used by the subsequent sensing pipeline.
- **Low-Complexity Vital Sign Processing Pipeline:** We propose a low-complexity end-to-end processing pipeline for vital sign estimation. This involves the identification of a persistent target-associated response in fast time, respiratory tracking in slow time, followed by cardiac-rate estimation. A low-complexity frequency-profile estimator is used for both fast-time response selection and slow-time respiratory tracking without covariance estimation or eigen decomposition. The resulting target-centric phase measurements are then used for cardiac rate estimation.
- **Experimental Physiological Validation:** We experimentally validate VitalFR3 using 16 human measurements, together with an end-expiratory apnea measurement. Our results demonstrate excellent agreement with the reference respiratory rates achieving a mean absolute error (MAE) of $0.758$ breaths per minute (BrPM) and the majority of the cardiac estimates are within $\pm 5$ BPM of the cardiac reference. The fine cardiac estimation was challenging in some measurements due to the presence of the respiratory signal's harmonics within the cardiac frequency range. We systematically characterize this respiratory harmonic ambiguity in the FR3 measurements using a fixed frequency criterion together with time–frequency inspection. Our analysis shows that respiratory harmonic proximity is associated with several of the larger cardiac estimation errors and quantifying it provides a confidence measure of the algorithm's results. The apnea measurement achieves a $0.2$ BPM MAE, providing additional evidence that cardiac-related motion is better recovered when respiratory harmonics are reduced.

The remainder of this paper is organized as follows. Section II reviews the relevant literature on FR3 measurement and radar-based physiological sensing. Section III describes the VitalFR3 measurement platform, waveform and acquisition design, and end-to-end calibration. Section IV presents the processing pipeline applied to the calibrated measurements. Section V presents the experimental physiological validation, including the baseline evaluation, apnea positive control, and respiratory-harmonic ambiguity assessment. Finally, Section VI concludes the paper.

## II. Related Work

Contactless vital sign sensing has been demonstrated using a range of RF platforms and operating frequencies. At sub-6 GHz, WiFi-based systems have used wireless channel measurements for respiration monitoring [4], [11]. Radar-based systems have also been used for respiratory and cardiac sensing at higher frequencies, including $24$ GHz Doppler radar [12], $60$ GHz frequency-modulated continuous-wave (FMCW) radar [13], and $77$ GHz FMCW radar [14]. These radar systems measure the small chest motions associated with respiration and heartbeat through changes in the received signal phase. FMCW radar platforms can also use range information to locate the target before extracting the physiological motion [13], [15]. Together, these studies show that contactless respiration and cardiac sensing can be performed across different RF bands and sensing architectures.

Recent work has also examined how practical measurement conditions affect radar-based vital sign sensing. Body motion can distort the phase variations used for respiratory and cardiac estimation, and several studies have developed methods for vital sign estimation in the presence of random or nonperiodic motion [15], [16]. Other work has combined multiple range bins and channels to improve cardiopulmonary signal recovery [14]. Robustness has also been studied under speaking conditions, where respiratory motion becomes less regular and the weaker cardiac component is more difficult to recover [17]. In addition to signal processing, front-end configuration can affect measurement quality; for example,

polarization mismatch has been shown to influence cardiac sensing accuracy in a 24 GHz Doppler radar system [12]. These studies show that reliable vital sign sensing depends on both physiological signal processing and the conditions under which the radar measurements are acquired. Prior studies relevant to FR3 have so far focused mainly on propagation, channel characterization, and, more recently, target sensing. Comparative ray-tracing studies have also examined FR3 propagation and coverage across suburban, urban, and high-rise urban environments [18], including cellular links in dense high-rise scenarios [19]. Xu et al. developed a channel model for FR3 extremely large-scale multiple-input multiple-output (XL-MIMO) systems that accounts for near-field propagation and spatial non-stationarity [20]. Indoor measurements at 6.75 and 16.95 GHz have characterized path loss and delay spread in office/laboratory and factory environments [5], [6]. Material penetration loss has also been measured across these frequencies [5]. Bomfin et al. examined multiband channel sensing at 6.5, 8.75, 10, and 15 GHz and evaluated the reliability of estimating channel components [9]. Moving from channel characterization toward target sensing, Pegoraro et al. studied coherent multiband ranging of object and human targets over 6–22 GHz [2]. At the network level, Shankar et al. investigated multistatic sensing in FR3, using geometry-aware multi-link fusion for target localization and velocity estimation [21]. Nieman et al. developed a reconfigurable FR3 channel sounder that supports monostatic and bistatic measurements and includes calibration of the transmit and receive measurement paths [8]. Experimental physiological sensing across FR3 remains limited, particularly for programmable measurement platforms that combine system characterization and calibration with respiratory and cardiac sensing across multiple FR3 center frequencies.

## III. VitalFR3 Measurement Platform, Waveform Design, and Calibration

VitalFR3 is implemented as a programmable FR3 measurement platform built around an Ettus USRP X440 and a SignalCraft SC2470 up/down converter. The X440 provides waveform generation and acquisition, while the SC2470 translates the signal to and from the selected FR3 center frequency. Because the recorded data contain the response and timing of the complete configured measurement path, this path is characterized and calibrated before the data are passed to the vital sign processing workflow of Section IV.

### A. FR3 Measurement Architecture and Signal Path

Figures 1 and 2a show the end-to-end VitalFR3 measurement chain and the corresponding physical implementation, respectively. The X440 complex in-phase/quadrature (I/Q) interface is operated at a sampling rate of 125 $\mathrm{MS/s}$ with a 1 GHz conversion rate. The X440–SC2470 interface is centered at an IF of 750 MHz in the VitalFR3 configuration. The SC2470 translates the IF signal to and from one selected FR3 RF center at a time. The platform architecture supports instantaneous bandwidths up to 1.6 GHz, while the measurements reported in this work use the fixed 100 MHz waveform configuration described below. The measurement campaign uses RF center frequencies of 10, 12.5, 15, 17.5, 20, and 22.5 GHz, with the same X440 sample plan and fixed receive path configuration retained for the calibration and radar measurements at each RF center.

TABLE I
VitalFR3 FMCW waveform and acquisition timing.

| Parameter | Value |
|---|---|
| Sweep direction | Up-chirp |
| Designed sweep bandwidth | 100 MHz |
| Designed complex I/Q chirp span | $-50$ to $+50$ MHz relative to IF |
| Active samples per chirp | 65,536 |
| Idle samples per chirp | 16,384 |
| Samples per CRI | 81,920 |
| Active chirp duration | 524.288 $\mu$s |
| Idle duration | 131.072 $\mu$s |
| CRI | 655.36 $\mu$s |
| Chirps per frame | 15 |
| Samples per frame | 1,228,800 |
| Frame duration | 9.8304 ms |
| Per-position slow-time rate | 101.725260 Hz |

The SC2470 is connected to separate transmit and receive Vivaldi-X ultra-wideband antennas mounted on a rigid custom acrylic fixture to maintain a fixed transmit–receive geometry throughout the measurements. On reception, the FR3 return is down-converted by the SC2470 to the IF domain and passes through the Mini-Circuits ZX75BP-750-S+ 600–900 MHz bandpass filter and a 6-dB attenuator before reaching the X440 receive interface. Both components form part of the fixed receive path. For the human measurements, the seated participant was positioned approximately 1 m in front of the antenna assembly, as shown in Fig. 2b.

Continuous I/Q samples are streamed between the X440 and a Linux host workstation through a 100 GbE QSFP56 connection using a dual-QSFP56 Mellanox ConnectX-6 Dx network interface, while a separate RJ45 link is used for device control. The acquisition workstation runs Ubuntu 24.04 LTS and is equipped with a 5.4 GHz Threadripper PRO 9975WX processor and 128 GB of ECC DDR5-5600 memory.

### B. FMCW Waveform and Acquisition Design

VitalFR3 employs a linear up-chirp FMCW waveform with a designed 100 MHz sweep bandwidth. At the X440 complex I/Q interface, the active chirp is designed to span $-50$ to $+50$ MHz relative to the 750 MHz IF center, corresponding to a 700–800 MHz IF sweep. The SC2470 translates this waveform to the selected FR3 RF center, and the realized waveform is verified directly from the recorded transmit samples later in this subsection.

The fixed waveform sample plan comprises 65,536 active samples and 16,384 idle samples per chirp, corresponding to a 524.288 $\mu$s active sweep and a chirp repetition interval (CRI) of 655.36 $\mu$s. Each frame contains 15 consecutive chirps and spans 9.8304 ms. The complete waveform and acquisition timing parameters are summarized in Table I.

For the nominal waveform design, let $B$ denote the designed sweep bandwidth and $T_{\mathrm{sw}}$ the active sweep duration. At the

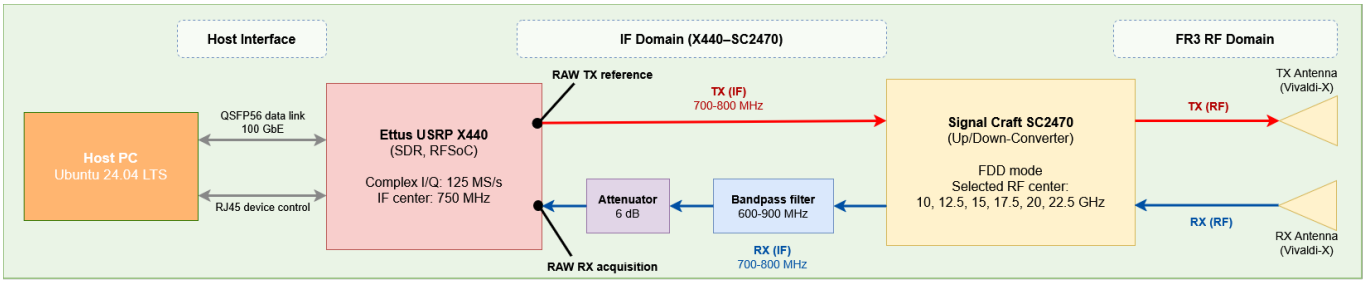



Fig. 1. End-to-end VitalFR3 hardware architecture and signal path.



(a) (b)

Fig. 2. VitalFR3 measurement platform: (a) hardware implementation comprising the Ettus USRP X440, SignalCraft SC2470, and fixed Vivaldi antenna assembly; (b) geometry used for the human measurements with the seated participant positioned approximately 1 m in front of the antenna assembly.

X440 complex I/Q interface, one transmitted up-chirp can be represented, apart from a constant complex amplitude, as

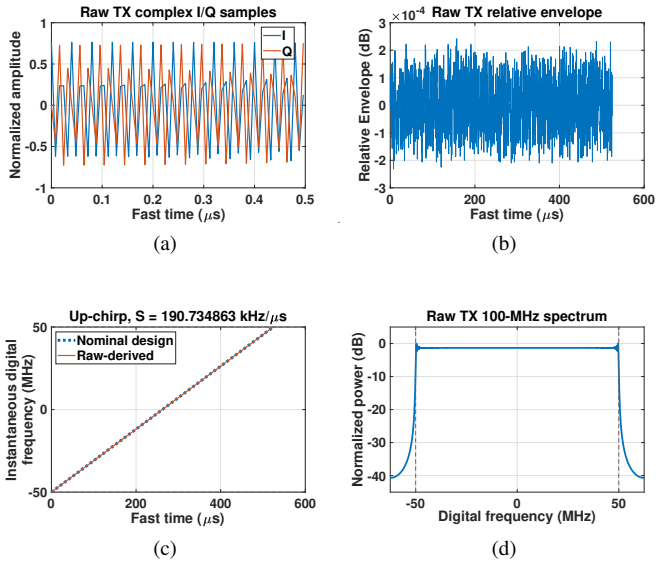
$$s_{\mathrm{IQ}}(t) = \exp\left\{ j2\pi \left[ -\frac{B}{2}t + \frac{1}{2}St^2 \right] \right\}, \qquad 0 \le t < T_{\mathrm{sw}}, \tag{1}$$

where $t$ is referenced to the start of the active sweep and $S = B/T_{\mathrm{sw}}$ is the designed FMCW chirp slope. For $B = 100$ MHz and $T_{\mathrm{sw}} = 524.288$ $\mu$s, the nominal slope is $S = 190.735$ kHz/$\mu$s.

Because the 15-chirp sample plan is repeated from frame to frame, each fixed chirp position recurs once every 9.8304 ms. Therefore, the samples associated with a given chirp position form a separate slow-time sequence with sampling rate $f_{\mathrm{slow}} = 101.725260$ Hz. The 15 chirp positions are retained as separate slow-time channels for subsequent target-centric processing rather than being concatenated into a single sequence at the chirp repetition rate.

The realized transmit waveform was verified directly from the raw complex I/Q transmit (TX) reference at the X440 interface, independently of the subsequent characterization of the complete measurement path. The recorded I/Q samples are shown in Fig. 3a, while Fig. 3b shows the corresponding complex envelope over the active sweep. Its magnitude remains effectively constant, with deviations confined to approximately $\pm 0.00024$ dB relative to the median. The instantaneous frequency in Fig. 3c closely follows the nominal linear design law over the complete active sweep. Fig. 3d confirms the intended 100 MHz digital spectral occupancy.

Quantitatively, the instantaneous frequency obtained from the raw data spans approximately $-50.000000$ to $+49.998474$ MHz over the active samples. The fitted slope




(a) (b) (c) (d)

Fig. 3. Raw transmit waveform verification at the X440 complex I/Q interface: (a) recorded complex I/Q samples; (b) transmit envelope relative to its median; (c) instantaneous frequency of the up-chirp; and (d) normalized digital power spectrum.

is 190.734863 kHz/$\mu$s, and the frequency span between the first and last active samples is 99.998474 MHz. This agrees with the designed 100 MHz chirp. The 65,536 active samples cover $0 \le t < T_{\mathrm{sw}}$, so the nominal span between the first and last samples is $B(65{,}535/65{,}536) = 99.998474$ MHz. The small difference from 100 MHz is therefore due to the discrete sample positions and does not indicate a reduction in the designed sweep bandwidth.

### C. Calibration of the Complete Measurement Path

Calibration was performed at the instrument level using raw I/Q data acquired with the antennas removed and the FR3 transmit and receive paths connected in loopback through a 30 dB attenuator, rather than by independently de-embedding individual components. For each of the six calibrated RF center frequencies, the complex transfer response of the configured measurement path was estimated from the raw RX acquisition relative to the raw TX reference over the measured chirp support. These two endpoints at the X440 interface are identified in Fig. 1. The installed ZX75BP-750-S+ receive filter is therefore included in the measured response of the

complete measurement path and is not separately inverted or de-embedded. The resulting complex response for each RF center provides the basis for the equalizer derived below.

Before estimating this response, the raw receive (RX) recordings were aligned and checked directly against the raw TX reference. An integer lag between RX and TX was first estimated by normalized complex correlation and then checked across multiple complete frames and chirp positions to verify that the alignment remained stable. The digital spectral orientation and dechirp sign were also verified directly from the raw loopback data rather than assumed from the nominal frequency plan. A test with a positive delay established $\mathrm{conj(RX)}$ TX as the dechirp convention used in the subsequent processing.

For each calibrated RF center frequency, the complex response was estimated from 15 segments distributed over the loopback recording, using chirps 1, 8, and 15 from five frame locations at fractions 0.05, 0.25, 0.50, 0.75, and 0.95 of the acquisition. After the validated integer alignment, the instantaneous complex response of each segment was formed as

$$H_{\mathrm{inst}}(f(t)) = \frac{x_{\mathrm{RX}}(t)}{x_{\mathrm{TX}}(t)}, \tag{2}$$

where $f(t)$ is the instantaneous digital frequency derived from the raw transmit chirp. An affine phase component was estimated from the unwrapped response phase over the central $\pm 40$ MHz reference region and removed from the response phase shape. The corresponding residual path delay obtained from the phase slope was retained for the electrical reference calculation described in Section III-D. The magnitude and residual phase responses were then summarized in 2048 frequency bins across the measured chirp support and combined across the 15 segments using the median.

Before constructing the equalizer, the repeatability of the measured response was evaluated across the 15 distributed segments at each RF center frequency. For every frequency bin, the standard deviation of the measured magnitude and residual phase was computed across the 15 segments. Repeatability thresholds were obtained from the central $\pm 40$ MHz reference region using the median plus six median absolute deviation (MAD) terms, with minimum thresholds of $0.10$ dB for magnitude and $1.50^\circ$ for phase. A bin was classified as calibratable only if its TX amplitude was no more than $1.5$ dB below the median TX amplitude over the central $\pm 40$ MHz reference region. Both repeatability measures also had to satisfy their respective thresholds. The response was accepted over the full band only when at least 99.9% of the measured chirp bins were calibratable and both bins at the chirp edges satisfied the same criteria. Up to four non-calibratable bins permitted by this acceptance policy were interpolated only for equalizer design, while the measured response itself was retained unchanged.

For equalizer design, the measured response was separated into its RF-dependent bulk gain and its frequency-dependent complex shape. The median magnitude over the symmetric measured chirp support was retained as the band gain for each RF center, while the corresponding normalized magnitude and residual phase shapes were used for correction. A constant phase term was likewise removed from the residual phase

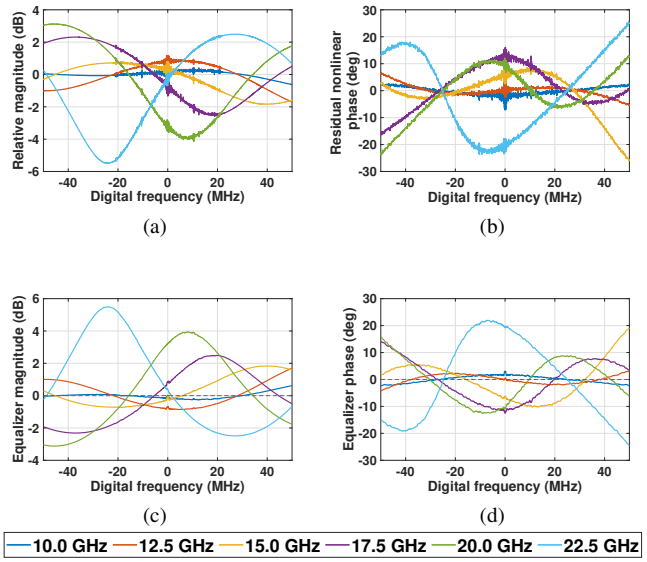



Fig. 4. Measured response of the complete measurement path and corresponding complex equalizer for each RF center over the measured chirp support: (a) measured magnitude shape relative to the preserved band gain; (b) measured residual nonlinear phase; (c) equalizer magnitude correction; (d) equalizer phase correction after removal of the affine component.

response. The resulting response shapes derived from the raw data exhibit RF-dependent magnitude and nonlinear phase structure across the measured chirp support, as shown in Figs. 4a and 4b. The response shapes used for equalizer construction were smoothed over a $0.75$ MHz span to form the complex response model $H_{\mathrm{m}}(f)$.

A regularized complex inverse was constructed as

$$E_\lambda(f) = \frac{H_{\mathrm{m}}^*(f)}{|H_{\mathrm{m}}(f)|^2 + \lambda}, \tag{3}$$

where $\lambda$ is the regularization parameter controlling the tradeoff between response flattening and excessive inverse gain in frequency regions where the measured response is weak. It was selected from 17 logarithmically spaced values over $10^{-8}$–$10^{0}$. For each candidate, the equalizer was normalized so that the median magnitude of the combined response over the symmetric measured chirp support was unity. Candidates whose maximum boost exceeded $6$ dB were rejected. Among the admissible candidates, the value of $\lambda$ minimizing the residual root-mean-square (RMS) magnitude error on the measured response shape was selected. Finally, the affine phase component of the selected equalizer was removed so that the equalizer corrected the nonlinear complex response shape without introducing an artificial bulk delay. The resulting equalizer magnitude and phase corrections for each RF center after removal of the affine component are shown in Figs. 4c and 4d, respectively.

### *D. Calibration Realization, Timing, and Electrical Reference*

For each RF center, the frequency-domain equalizer was implemented as a 257-tap causal complex finite impulse response (FIR) filter. The equalizer correction was applied over the full

TABLE II
TIMING AND ELECTRICAL REFERENCE PARAMETERS AT EACH RF CENTER.

| RF center (GHz) | $D_{\mathrm{HW}}$ (samples) | $\tau_0$ (ns) | $f_0$ (Hz) |
|---|---|---|---|
| 10 | 404 | −3.331238 | −635.383174 |
| 12.5 | 404 | −3.714944 | −708.569410 |
| 15 | 403 | +3.743185 | +713.955946 |
| 17.5 | 404 | −2.742069 | −523.008190 |
| 20 | 404 | −2.102393 | −400.999729 |
| 22.5 | 404 | −2.741170 | −522.836606 |

measured chirp support and was smoothly transitioned to unity outside the chirp band, reaching unity by $|f| = 60$ MHz. The FIR introduces a fixed delay of $D_{\mathrm{FIR}} = 128$ samples, corresponding to $1.024$ $\mu$s at $125$ MS/s, which is compensated after filtering. The filters are applied continuously, with their state preserved across processing blocks to avoid boundary transients.

The coarse RX–TX sample alignment established from the raw loopback measurements is represented by the integer delay $D_{\mathrm{HW}}$ for each RF center. It accounts for the fixed sample offset between the transmit and receive paths and is distinct from the 128-sample delay $D_{\mathrm{FIR}}$ introduced by the causal calibration FIR. The two delays are therefore compensated separately.

After the integer RX–TX alignment, a small residual linear phase slope remained in the loopback response. For each RF center, the slope was estimated from the unwrapped loopback phase $\phi(f)$ over the central $\pm 40$ MHz reference region and converted to a fractional electrical delay

$$\tau_0 = -\frac{1}{2\pi}\frac{d\phi}{df}. \tag{4}$$

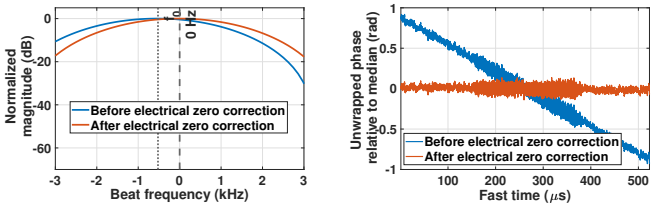
The reported value of $\tau_0$ was taken as the median over the same 15 distributed loopback segments used to characterize the complex response. Using the chirp slope $S$ derived from the raw transmit data, the corresponding electrical beat-frequency offset for each RF center was defined as

$$f_0 = S\tau_0. \tag{5}$$

The resulting values of $D_{\mathrm{HW}}$, $\tau_0$, and $f_0$ for the six calibrated RF centers are summarized in Table II. At 15 GHz, $\tau_0$ changes sign because $D_{\mathrm{HW}}$ changes by one sample, leaving the residual fractional delay with the opposite sign. This sign change does not indicate a negative physical delay or noncausal behavior.

The offset $f_0$ for each RF center is applied after dechirping to establish the electrical beat-frequency zero before subsequent fast-time processing. This calibration defines only an electrical loopback zero reference; it does not establish an absolute physical range origin at the antenna aperture. Its effect is illustrated for a representative 22.5 GHz loopback measurement in Fig. 5, where the correction removes the residual beat-frequency offset and the corresponding linear phase slope.

After dechirping and application of the electrical zero correction for each RF center, the complex fast-time signal was




(a) (b)

Fig. 5. Representative electrical zero correction at 22.5 GHz: (a) beat frequency before and after correction; (b) corresponding phase slope before and after correction.

passed through a four-stage anti-aliasing (AA) and decimation chain. The successive decimation factors were 4, 4, 4, and 2, giving an overall decimation factor of 128 and reducing the sampling rate from 125 MS/s to 976.5625 kS/s. This produces 512 complex fast-time samples over each active chirp while retaining the validated beat-frequency band $|f_b| \leq 300$ kHz, where $f_b$ denotes the beat frequency after the electrical zero correction. The delay introduced by each AA stage was removed before the next stage, leaving no residual delay from the AA filters in the final output. This AA and decimation chain is distinct from the 257-tap calibration FIR described above.

### E. Calibration Performance

The final calibration was assessed in two ways. Across the same 15 distributed loopback segments used for calibration characterization, all six RF centers had at least 99.95117% calibratable frequency bins. The RMS error in magnitude shape after correction remained below 0.061 dB across the calibrated band, compared with uncorrected values reaching 2.836 dB. The finite 257-tap FIR realization was also compared with the corresponding frequency-domain equalizer target. Across the six RF centers, the worst-case errors were 0.00466 dB in magnitude and 0.04621° in phase. The results for each RF center are summarized in Table III.

The FMCW waveform was further evaluated in the time–frequency domain at all six RF centers. Fig. 6 shows the 22.5 GHz loopback measurement as a representative example. The calibrated RX signal preserves the positive slope of the raw TX chirp and closely follows the frequency law fitted to the raw TX data. Across the six RF centers, the measured chirp slopes differed from the raw TX reference slope by only a few parts per million. The anti-aliasing and decimation chain was also validated over the retained beat-frequency band $|f_b| \leq 300$ kHz, with a cascade passband ripple of 0.00370 dB and a worst-case alias-folding level of approximately −79.14 dB.

After calibration and decimation, each acquisition is represented by calibrated complex fast-time data. These data form the input to the vital sign processing workflow described in the next section.

## IV. VITAL SIGN PROCESSING PIPELINE

The calibrated complex fast-time data from Section III are processed using the workflow shown in Fig. 7. The workflow

TABLE III
CALIBRATION PERFORMANCE AND FIR REALIZATION ACCURACY AT THE SIX RF CENTER FREQUENCIES.

| RF center (GHz) | Calibratable fraction (%) | $\lambda$ (in Eq. 3) | Maximum equalizer boost (dB) | RMS error in magnitude shape (dB) | | FIR realization RMS Magnitude (dB) / Phase (°) |
|---|---|---|---|---|---|---|
| | | | | Before | After | |
| 10.0 | 100.00000 | $1.0 \times 10^{-8}$ | 0.6162 | 0.20088 | 0.06048 | 0.00394 / 0.04621 |
| 12.5 | 100.00000 | $3.1623 \times 10^{-7}$ | 1.6764 | 0.73662 | 0.04073 | 0.00280 / 0.02794 |
| 15.0 | 99.95117 | $1.0 \times 10^{-8}$ | 1.8359 | 0.98115 | 0.06033 | 0.00431 / 0.03923 |
| 17.5 | 99.95117 | $1.0 \times 10^{-8}$ | 2.4908 | 1.70931 | 0.05902 | 0.00466 / 0.04047 |
| 20.0 | 99.95117 | $1.0 \times 10^{-8}$ | 3.9476 | 2.36207 | 0.04763 | 0.00324 / 0.04166 |
| 22.5 | 100.00000 | $1.0 \times 10^{-8}$ | 5.4854 | 2.83575 | 0.04115 | 0.00326 / 0.04108 |

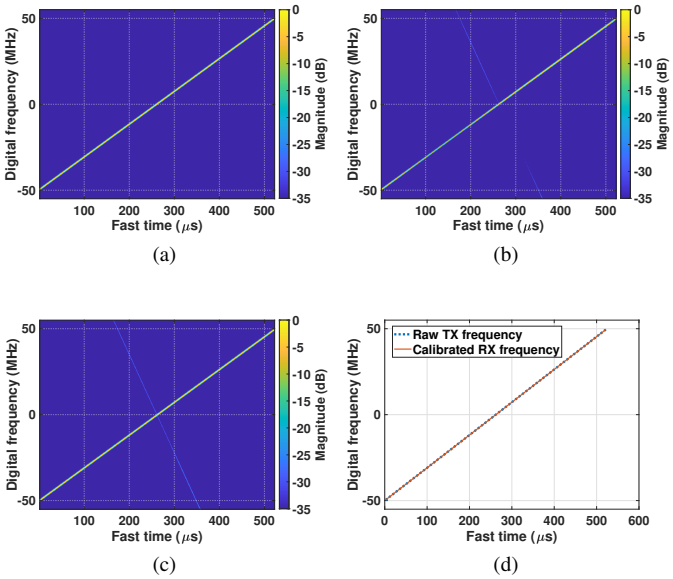



Fig. 6. End-to-end time–frequency validation using a representative 22.5 GHz loopback measurement: (a) raw TX spectrogram; (b) aligned raw RX spectrogram; (c) RX spectrogram after the final calibration FIR; and (d) comparison of the raw TX fitted frequency law with the calibrated RX frequency trajectory.

first localizes a persistent target response in fast-time, then tracks respiration and estimates the cardiac component from the corresponding slow-time measurements.

### A. Calibrated Fast-Time Input and Static Clutter Suppression

For each acquisition, the calibrated complex fast-time samples are organized as

$$\mathcal{X} = \{x_{m,c,p}\} \in \mathbb{C}^{N_s \times N_c \times N_f}, \qquad N_s = 512, \quad N_c = 15, \tag{6}$$

where $m$, $c$, and $p$ denote the fast-time sample, chirp position, and frame indices, respectively, and $N_f$ is the number of acquired frames. The chirp positions are retained as separate observations through the subsequent processing stages.

Static clutter is suppressed along the frame dimension using a forward–backward exponentially weighted moving average (EWMA) with $\alpha_c = 0.005$. Applying the EWMA in both temporal directions avoids introducing a systematic phase delay into the slow-time sequences. The resulting data cube after clutter suppression, $\widetilde{\mathcal{X}} \in \mathbb{C}^{N_s \times N_c \times N_f}$, is used as the input to the fast-time persistent target response localization described below.

### B. Adopted Frequency-Profile Estimator

VitalFR3 uses frequency estimation at two stages of the processing workflow: fast-time localization of the persistent target response and slow-time tracking of respiration. For both tasks, we adopt our previously developed frequency-profile estimator [4]. The estimator operates directly on the observation snapshots and does not require explicit covariance estimation or eigen decomposition. Its dominant computational cost scales linearly with the number of frequency grid points, snapshots, and temporal samples. These properties make the estimator suitable for repeated use in both processing stages, while its behavior with nonstationary respiratory signals is particularly relevant to respiratory tracking. For input snapshots $\mathbf{Y}$ and a prescribed frequency grid $\mathcal{G} = \{f^{(0)}, \ldots, f^{(K-1)}\}$, we denote the estimator output by

$$\mathbf{\Phi} = \mathcal{E}_{\mathrm{FP}}\left(\mathbf{Y}; \mathcal{G}, \mu\right), \tag{7}$$

where $\mathbf{\Phi} = [\Phi_0, \ldots, \Phi_{K-1}]^T$ is the resulting frequency profile and $\mu$ is the estimator step size. The frequency estimate is obtained from the maximum of the profile as

$$\widehat{f} = f^{(k^\star)}, \qquad k^\star = \arg \max_{k \in \{0,\ldots,K-1\}} \Phi_k. \tag{8}$$

Further details of the estimator formulation and implementation are provided in [4]; here, we use the estimator through the frequency-profile interface defined above.

### C. Persistent Beat-Frequency Localization and Target-Centric Projection

For fast-time localization, the $N_c = 15$ clutter-suppressed chirps in each frame $p$ are treated as separate fast-time snapshots. The snapshot corresponding to chirp position $c$ is written as

$$\widetilde{\mathbf{x}}_{c,p} = [\widetilde{x}_{0,c,p}, \widetilde{x}_{1,c,p}, \ldots, \widetilde{x}_{N_s-1,c,p}]^T \in \mathbb{C}^{N_s}, \tag{9}$$

and the set of snapshots for frame $p$ is

$$\mathbf{Y}_p^{\mathrm{FT}} = \{\widetilde{\mathbf{x}}_{c,p}\}_{c=1}^{N_c}. \tag{10}$$

The superscript FT denotes fast-time observations.

The fast-time search grid $\mathcal{G}_{\mathrm{FT}}$ spans 0.5–10 kHz with $K_{\mathrm{FT}} = 1000$ candidate frequencies. Applying the frequency-profile estimator to $\mathbf{Y}_p^{\mathrm{FT}}$ with $\mu_{\mathrm{FT}} = 0.1$ produces the fast-time profile $\mathbf{\Phi}_p^{\mathrm{FT}}$. The corresponding frame-wise estimate of the target beat frequency, $\widehat{f}_{b,p}$, is obtained from the profile maximum.

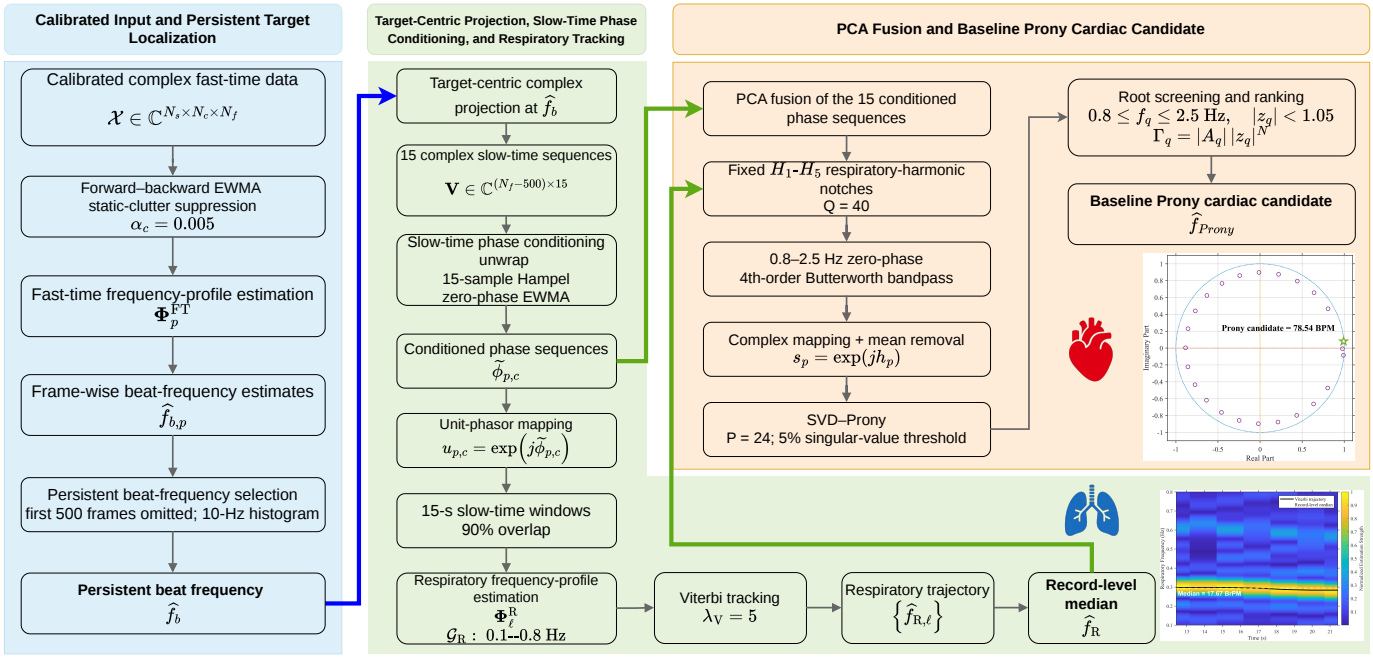



Fig. 7. VitalFR3 processing workflow from calibrated fast-time data to respiratory tracking and the baseline Prony cardiac candidate.

To exclude the initial acquisition transient, the first 500 frames, corresponding to approximately 4.9 s, are omitted when selecting the persistent target. The retained frame-wise estimates $\{\widehat{f}_{b,p}\}$ are then grouped using 10 Hz histogram bins, and the center frequency of the most populated bin is selected as the persistent target beat frequency, denoted by $\widehat{f}_b$. This aggregation reduces the influence of isolated frame-wise deviations.

Once the persistent target beat frequency $\widehat{f}_b$ has been identified, each retained chirp is projected at this frequency to obtain a target-centric complex measurement. For chirp position $c$ in frame $p$, the complex projection is

$$v_{p,c} = \sum_{m=0}^{N_s-1} \widetilde{x}_{m,c,p} \exp\left(-j2\pi \widehat{f}_b m T_s^d\right), \tag{11}$$

where $T_s^d$ is the fast-time sampling interval after decimation. The resulting target-centric complex measurements are arranged as the two-dimensional matrix $\mathbf{V} = [v_{p,c}] \in \mathbb{C}^{(N_f-500)\times N_c}$, where the rows correspond to the retained frames and the columns correspond to the $N_c = 15$ chirp positions. Each column of $\mathbf{V}$ therefore forms a separate complex slow-time sequence associated with a fixed chirp position.

### D. Slow-Time Phase Conditioning and Respiratory Tracking

The phase of each column of $\mathbf{V}$ is independently unwrapped along slow-time and processed with a 15-sample Hampel filter to suppress impulsive deviations. Slow baseline variations are then removed using a zero-phase EWMA with $\alpha_\phi = 0.00215513$, selected to limit attenuation at the lower edge of the respiratory band (0.1 Hz) to approximately 1 dB. The forward–backward implementation avoids introducing a systematic phase shift into the conditioned slow-time sequences. The resulting phase samples are denoted by $\widetilde{\phi}_{p,c}$.

For respiratory frequency estimation, the conditioned phase samples are mapped to unit-modulus complex phasors,

$$u_{p,c} = \exp\left(j\widetilde{\phi}_{p,c}\right). \tag{12}$$

The resulting $N_c = 15$ slow-time sequences are retained separately and used as the observations for respiratory frequency tracking.

A sliding window of 15 s with 90% overlap is applied to the slow-time sequences in (12). Let $W$ denote the number of slow-time samples in each window and let $p_\ell$ denote the starting frame of the $\ell$th window. For chirp position $c$, the corresponding slow-time snapshot is

$$\mathbf{u}_{c,\ell} = [u_{p_\ell,c}, u_{p_\ell+1,c}, \ldots, u_{p_\ell+W-1,c}]^T \in \mathbb{C}^W, \tag{13}$$

and the set of observations for that window is

$$\mathbf{Y}_\ell^{\mathrm{ST}} = \{\mathbf{u}_{c,\ell}\}_{c=1}^{N_c}. \tag{14}$$

Here, the superscript ST denotes slow-time observations.

The respiratory search grid $\mathcal{G}_{\mathrm{R}} = \{f_{\mathrm{R}}^{(k)}\}_{k=0}^{K_{\mathrm{R}}-1}$ spans 0.1–0.8 Hz with $K_{\mathrm{R}} = 800$ candidate frequencies. For each slow-time window $\ell$, the frequency-profile estimator is applied to $\mathbf{Y}_\ell^{\mathrm{ST}}$ with $\mu_{\mathrm{R}} = 0.1$ to obtain the respiratory frequency profile $\mathbf{\Phi}_\ell^{\mathrm{R}}$.

Before Viterbi tracking, the complete respiratory frequency-profile map is normalized by its global maximum. Let $\overline{\Phi}_{\ell,k}^{\mathrm{R}}$ denote the normalized profile value at candidate frequency

$f_{\mathrm{R}}^{(k)}$ in the $\ell$th window, and let $J_{\ell,k}$ denote the cumulative path score. The Viterbi recursion is

$$\begin{aligned} J_{1,k} &= \overline{\Phi}_{1,k}^{\mathrm{R}}, \\ J_{\ell,k} &= \overline{\Phi}_{\ell,k}^{\mathrm{R}} \\ &\quad + \max_{0\le k'<K_{\mathrm{R}}} \Big[ J_{\ell-1,k'} \\ &\qquad - \lambda_{\mathrm{V}} \left| f_{\mathrm{R}}^{(k)} - f_{\mathrm{R}}^{(k')} \right| \Big]. \end{aligned} \tag{15}$$

The recursion is applied for $\ell \ge 2$, and $\lambda_{\mathrm{V}} = 5\ \mathrm{Hz}^{-1}$ is the transition penalty weight. Backtracking from the maximum terminal score gives the optimal state sequence $\{\widehat{k}_\ell\}$, from which the respiratory frequency trajectory is $\widehat{f}_{\mathrm{R},\ell} = f_{\mathrm{R}}^{(\widehat{k}_\ell)}$. A representative respiratory frequency for the complete acquisition is then obtained as

$$\widehat{f}_{\mathrm{R}} = \mathrm{median}_\ell \left\{ \widehat{f}_{\mathrm{R},\ell} \right\}. \tag{16}$$

### *E. Principal Component Fusion, Respiratory Harmonic Suppression, and Baseline Prony Candidate*

The mean is first removed from each of the $N_c = 15$ conditioned phase sequences, and principal component analysis (PCA) is then applied to the resulting phase matrix. The first principal component is retained as the fused phase observation. Its polarity is aligned with the sample-wise mean of the 15 conditioned phase sequences, and its amplitude is rescaled to match the standard deviation of that mean.

Respiratory harmonics are suppressed using five notch filters centered at $f_{\mathrm{H},n} = n\widehat{f}_{\mathrm{R}}$, $n = 1, \ldots, 5$. Each notch has a quality factor of $Q = 40$. The filters are designed once per acquisition using the representative respiratory frequency $\widehat{f}_{\mathrm{R}}$ and then applied to the fused phase observation. After notch filtering, the fused phase observation is band-limited to 0.8–2.5 Hz using a fourth-order Butterworth filter applied in forward–backward form. The resulting real-valued sequence is denoted by $h_p$.

For Prony analysis, the filtered phase sequence is first mapped to a unit-modulus complex sequence,

$$s_p = \exp(j h_p), \tag{17}$$

after which its sample mean is removed to obtain $\widetilde{s}_p$. A linear prediction model of order $P = 24$ is then fitted according to

$$\widetilde{s}_p + \sum_{r=1}^{P} a_r \widetilde{s}_{p-r} \approx 0, \tag{18}$$

where $p$ indexes the slow-time samples, $r$ is the lag index, and $a_r$ is the corresponding complex linear prediction coefficient. The coefficients $\{a_r\}_{r=1}^{P}$ are obtained from the corresponding least-squares system using singular value decomposition (SVD) regularization, retaining singular values greater than 5% of the largest singular value.

The roots of the fitted prediction polynomial,

$$z^P + \sum_{r=1}^{P} a_r z^{P-r} = 0, \tag{19}$$

define the Prony modes. For the $q$th nonzero root $z_q$, let $\mathrm{Arg}(z_q) \in (-\pi, \pi]$ denote its principal phase. The corresponding modal frequency is

$$f_q = \frac{f_{\mathrm{slow}}}{2\pi} \left| \mathrm{Arg}(z_q) \right|, \tag{20}$$

where $f_{\mathrm{slow}}$ is the slow-time sampling rate. Only roots satisfying $0.8 \le f_q \le 2.5$ Hz and $0 < |z_q| < 1.05$ are retained as candidates in the cardiac band.

The complex modal amplitudes $A_q$ are obtained by least-squares fitting of the Prony modes to $\widetilde{s}_p$. Each valid root is then ranked using

$$\Gamma_q = |A_q|\, |z_q|^N, \tag{21}$$

where $N$ is the number of slow-time samples used in the Prony analysis. The valid root with the largest $\Gamma_q$ defines the baseline Prony cardiac candidate, whose frequency is denoted by $\widehat{f}_{\mathrm{Prony}}$. Algorithm 1 summarizes the steps described above.

## V. Experimental Physiological Validation

The processing workflow described in Section IV is evaluated using 16 radar measurement records. A separate end-expiratory apnea acquisition is examined as a positive control. We also characterize cases in which the Prony cardiac candidate approaches respiratory harmonics.

### *A. Experimental Data, References, and Evaluation Roles*

The evaluation comprises 16 radar measurement records, identified as Records 01–16. All records were acquired from a single participant in separate acquisitions spanning different days and times of day. Clothing and environmental conditions varied across the measurements. The record identifiers are used only to distinguish the measurements and do not indicate their temporal acquisition order.

The measurements were conducted in an indoor laboratory of approximately 50 $\mathrm{m}^2$, with the participant seated approximately 1 m from the radar, as described in Section III. Respiratory reference measurements were acquired using a Vernier Go Direct Respiration Belt, while the cardiac reference was obtained from electrocardiogram (ECG) recordings acquired with an Analog Devices MAX-ECG-MONITOR. For record-level respiratory evaluation, the signal from the respiration belt was detrended and passed through a low-pass filter. The dominant spectral component within the respiratory frequency range served as the reference respiratory frequency. For each record, the cardiac reference was the median heart rate from the corresponding ECG recording.

The physiological reference signals were not used in the radar processing described in Section IV. The radar and physiological reference sensors did not share a common acquisition trigger or time base. Therefore, we compare the respiratory and cardiac rates for each recording rather than individual beats or samples.

A separate end-expiratory apnea acquisition was collected as a positive control. It is not included among Records 01–16.

**Algorithm 1** VitalFR3 vital sign processing workflow

**Require:** Calibrated complex fast-time data
**Ensure:** $\widehat{f}_{\mathrm{R}}$, $\widehat{f}_{\mathrm{Prony}}$

Form $\mathcal{X}$; suppress static clutter ($\alpha_c = 0.005$) to obtain $\widetilde{\mathcal{X}}$
**for** each frame $p$ **do**
  Form $\mathbf{Y}_p^{\mathrm{FT}}$ using Eq. 10
  Apply Eqs. 7 and 8 with $\mu_{\mathrm{FT}} = 0.1 \rightarrow \widehat{f}_{b,p}$
**end for**
Discard the first 500 frames
$\widehat{f}_b \leftarrow$ center of the most populated 10-Hz histogram bin
**for** each retained $(p, c)$ **do**
  Compute $v_{p,c}$ using Eq. 11
**end for**
$\mathbf{V} \leftarrow [v_{p,c}]$
**for** each chirp position $c$ **do**
  Unwrap the phase of $v_{p,c}$; Hampel filter (15 samples)
  Zero-phase EWMA ($\alpha_\phi = 0.00215513$) $\rightarrow \widetilde{\phi}_{p,c}$
  $u_{p,c} \leftarrow \exp(j\widetilde{\phi}_{p,c})$
**end for**
**for** each 15-s slow-time window $\ell$ with 90% overlap **do**
  Form $\mathbf{Y}_\ell^{\mathrm{ST}}$ using Eq. 14
  Apply Eq. 7 with $\mu_{\mathrm{R}} = 0.1 \rightarrow \mathbf{\Phi}_\ell^{\mathrm{R}}$
**end for**
Obtain $\{\widehat{f}_{\mathrm{R},\ell}\}$ by Viterbi tracking using Eq. 15
Compute $\widehat{f}_{\mathrm{R}}$ using Eq. 16
Mean-center the $N_c$ conditioned phase sequences and apply PCA
Align and rescale the first principal component
Apply notch filters at $f_{\mathrm{H},n} = n\widehat{f}_{\mathrm{R}}$, $n = 1, \ldots, 5$, with $Q = 40$
Apply a fourth-order Butterworth filter over 0.8–2.5 Hz in forward–backward form $\rightarrow h_p$
$s_p \leftarrow \exp(jh_p)$
Remove the sample mean from $s_p$ to obtain $\widetilde{s}_p$
Fit Eq. 18 with $P = 24$; retain singular values $> 5\%$ of the largest
Compute $z_q$ from Eq. 19
Compute $f_q$ using Eq. 20
Estimate $A_q$ by least-squares fitting of the Prony modes to $\widetilde{s}_p$
Retain $0.8 \le f_q \le 2.5$ Hz, $0 < |z_q| < 1.05$
Rank valid roots using Eq. 21
$\widehat{f}_{\mathrm{Prony}} \leftarrow$ frequency of the highest-ranked valid root

### B. Baseline Vital Sign Performance

Table IV summarizes the respiratory and cardiac results for all 16 measurements. The respiratory rate estimates had an MAE of 0.758 BrPM and a median absolute error of 0.472 BrPM. In 15 of the 16 records, the absolute respiratory error was no greater than 1.114 BrPM. Record 03 was the exception, with an absolute error of 4.585 BrPM. For cardiac estimation, the baseline Prony candidate was within ±5 BPM of the ECG reference in 11 of the 16 records (68.75%). Across all records, the cardiac MAE was 4.650 BPM, the median absolute error was 3.424 BPM, and the maximum absolute error was 15.586 BPM.

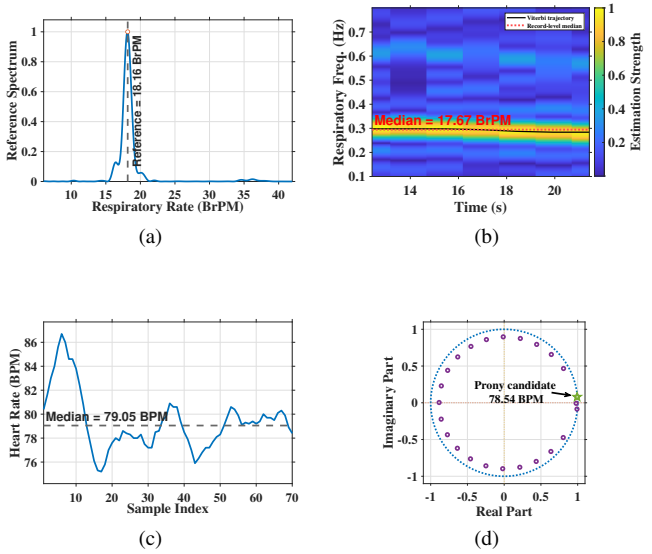



Fig. 8. Representative baseline results for Record 01 at 10 GHz: (a) spectrum of the signal from the respiration belt, (b) radar respiratory frequency profile with the Viterbi trajectory and median estimate for the record, (c) heart rate from the ECG recording with its median value, and (d) Prony roots in the $z$-plane with the selected baseline Prony candidate.

Fig. 8 illustrates the baseline processing results for Record 01 at 10 GHz. The respiratory rate estimated from the radar was 17.670 BrPM, compared with 18.164 BrPM from the respiration belt. The baseline Prony cardiac candidate was 78.536 BPM, while the corresponding ECG reference was 79.050 BPM.

### C. End-Expiratory Apnea Positive Control

A narrow bandpass filter can make even noise appear as a regular oscillation. Therefore, a waveform that resembles cardiac activity only after cardiac-band filtering does not by itself provide convincing evidence that the corresponding component was present in the radar measurements before filtering. For this reason, a separate end-expiratory apnea acquisition was used as a positive control. We examined the calibrated radar phase without cardiac-band filtering to determine whether a common component was present before cardiac filtering.

After a normal exhalation, the participant held their breath for approximately 20 s. This substantially reduced periodic chest motion caused by respiration during the analyzed interval. The $N_c = 15$ calibrated phase sequences were examined without respiratory harmonic notching or cardiac-band filtering. PCA was then applied directly to these phase observations. Let $\lambda_1 \ge \lambda_2 \ge \cdots \ge \lambda_{15}$ denote the PCA eigenvalues. The normalized variance contribution of the $i$th principal component is

$$\eta_i = \frac{\lambda_i}{\sum_{j=1}^{15} \lambda_j}. \tag{22}$$

Fig. 9 shows the normalized PCA eigenvalue distribution. The first principal component accounted for 25.9% of the total

TABLE IV
RECORD-LEVEL BASELINE RESPIRATORY AND CARDIAC PERFORMANCE. PHYSIOLOGICAL REFERENCES ARE USED ONLY FOR POST HOC EVALUATION.

| Record | RF | Respiration (BrPM) | | | Cardiac (BPM) | | |
|---|---|---|---|---|---|---|---|
| | (GHz) | Reference | Radar | Abs. error | ECG reference | Prony candidate | Abs. error |
| 01 | 10 | 18.164 | 17.670 | 0.494 | 79.050 | 78.536 | 0.514 |
| 02 | 12.5 | 18.677 | 18.563 | 0.114 | 87.000 | 74.918 | 12.082 |
| 03 | 17.5 | 18.604 | 23.189 | 4.585 | 85.900 | 86.719 | 0.819 |
| 04 | 20 | 18.677 | 18.038 | 0.639 | 86.000 | 92.607 | 6.607 |
| 05 | 10 | 18.237 | 19.194 | 0.957 | 91.200 | 80.202 | 10.998 |
| 06 | 12.5 | 18.823 | 18.195 | 0.628 | 90.100 | 83.625 | 6.475 |
| 07 | 15 | 18.750 | 18.300 | 0.450 | 90.400 | 74.814 | 15.586 |
| 08 | 17.5 | 18.530 | 18.143 | 0.388 | 89.900 | 94.589 | 4.689 |
| 09 | 20 | 18.237 | 19.352 | 1.114 | 88.900 | 87.614 | 1.286 |
| 10 | 22.5 | 18.970 | 18.458 | 0.512 | 88.750 | 89.726 | 0.976 |
| 11 | 10 | 21.753 | 21.612 | 0.141 | 93.800 | 89.038 | 4.762 |
| 12 | 12.5 | 20.654 | 19.667 | 0.987 | 93.600 | 94.292 | 0.692 |
| 13 | 15 | 19.189 | 19.089 | 0.101 | 92.700 | 94.705 | 2.005 |
| 14 | 17.5 | 19.702 | 19.299 | 0.403 | 91.800 | 91.862 | 0.062 |
| 15 | 20 | 19.336 | 19.615 | 0.279 | 91.000 | 87.844 | 3.156 |
| 16 | 22.5 | 19.482 | 19.825 | 0.342 | 90.800 | 87.108 | 3.692 |

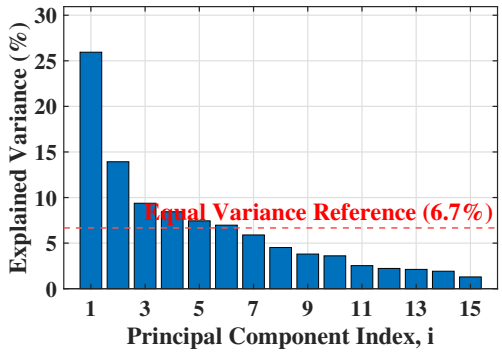



Fig. 9. Normalized variance contributions of the 15 principal components during end-expiratory apnea. The dashed line denotes the equal-variance reference of $1/15 \approx 6.7\%$.

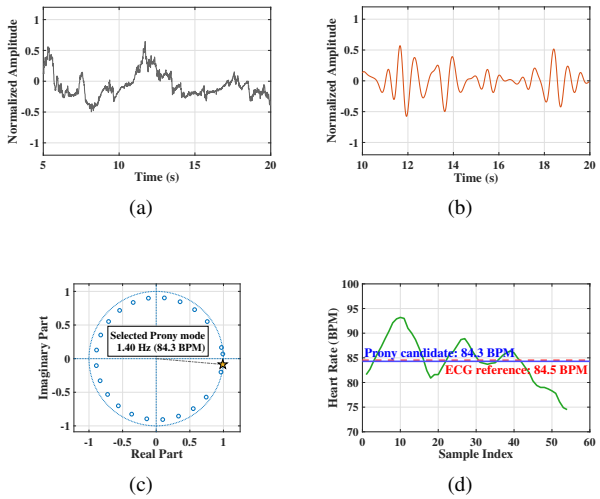



Fig. 10. End-expiratory apnea positive control: (a) phase observation, (b) waveform after baseline cardiac processing, (c) Prony roots in the $z$-plane, and (d) heart rate from the ECG recording.

variance. If the variance were distributed equally among the 15 components, each component would account for $1/15 \approx 6.7\%$. The larger contribution of the first principal component indicates that the phase observations contained a common component. The $6.7\%$ value is used only as an equal variance reference and not as a statistical threshold for rejecting white noise.

Fig. 10 shows the cardiac results from the apnea acquisition. The baseline cardiac processing yielded the recovered waveform and a Prony cardiac candidate of $84.3$ BPM. The ECG reference for this acquisition was approximately $84.5$ BPM. The radar cardiac estimate closely agrees with the ECG reference. This supports the presence of cardiac-related motion in the radar measurements before cardiac filtering.

### *D. Respiratory Harmonic Ambiguity Assessment*

Respiratory motion is not purely sinusoidal and contains harmonic components [22] that can extend into the frequency range occupied by cardiac motion. When a respiratory harmonic approaches the cardiac frequency, it can interfere with cardiac estimation and make the physiological origin of a frequency component ambiguous. Respiratory harmonic interference has been widely reported in radar vital sign sensing, with mitigation methods including high-resolution parametric estimation, adaptive multistage harmonic suppression, cyclostationary harmonic suppression, and phase-difference processing [13], [23], [24]. This behavior is also observed in our measurements, where the Prony cardiac candidate approaches harmonics of the tracked respiratory frequency in several records. Harmonic suppression or separation is outside the scope of this work. We instead characterize the observed ambiguity in terms of its frequency proximity, persistence over the record, and time–frequency behavior.

To quantify this ambiguity, we compare the record-level Prony cardiac candidate with the respiratory harmonics computed from the respiratory trajectory tracked by Viterbi. Because the harmonic frequencies change with the respiratory trajectory, this separation is evaluated in each slow-time anal-

TABLE V
PROXIMITY OF THE PRONY CANDIDATE TO THE EXAMINED RESPIRATORY HARMONICS ACROSS THE 16 MEASUREMENT RECORDS.

| Record | Harmonic order at $\varepsilon_{\min}$ | $\varepsilon_{\min}$ (Hz) | $\rho_{\mathrm{col}}$ (%) |
|---|---|---|---|
| 01 | H5 | 0.1109 | 0.000 |
| 02 | H4 | 0.0040 | 100.000 |
| 03 | H4 | 0.0130 | 42.857 |
| 04 | H5 | 0.0403 | 100.000 |
| 05 | H4 | 0.0220 | 100.000 |
| 06 | H5 | 0.1006 | 0.000 |
| 07 | H4 | 0.0268 | 100.000 |
| 08 | H5 | 0.0645 | 71.429 |
| 09 | H5 | 0.1480 | 0.000 |
| 10 | H5 | 0.0076 | 100.000 |
| 11 | H4 | 0.0094 | 100.000 |
| 12 | H5 | 0.0673 | 100.000 |
| 13 | H5 | 0.0123 | 100.000 |
| 14 | H5 | 0.0509 | 57.143 |
| 15 | H5 | 0.1310 | 0.000 |
| 16 | H4 | 0.1301 | 0.000 |

ysis window. For the $\ell$th window, the distance from the Prony candidate to the nearest examined respiratory harmonic is defined as

$$\varepsilon_\ell = \min_{h\in\{3,\dots,8\}} \left| \widehat{f}_{\mathrm{Prony}} - h\widehat{f}_{\mathrm{R},\ell} \right|. \tag{23}$$

A window is counted as a collision when the nearest harmonic lies within a fixed frequency guard of the Prony candidate,

$$\varepsilon_\ell \le \varepsilon_0, \qquad \varepsilon_0 = 0.08 \text{ Hz}, \tag{24}$$

where the guard $\varepsilon_0$ is used only as an operational criterion for geometric proximity. The $0.08$ Hz guard corresponds to $4.8$ BPM, close to the $5$ BPM tolerance used for cardiac error in Section V-B. For a record containing $N_{\mathrm{win}}$ slow-time analysis windows, the collision occupancy is defined as

$$\rho_{\mathrm{col}} = \frac{100}{N_{\mathrm{win}}} \sum_{\ell=1}^{N_{\mathrm{win}}} \mathbb{I}\left(\varepsilon_\ell \le \varepsilon_0\right), \tag{25}$$

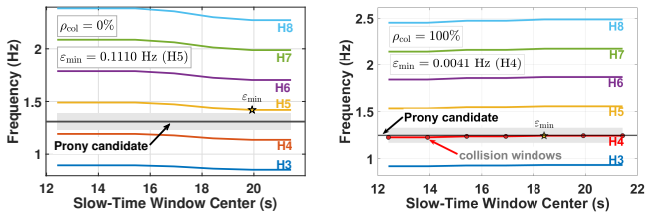
where $\mathbb{I}(\cdot)$ denotes the indicator function. The minimum distance over all slow-time analysis windows in the record,

$$\varepsilon_{\min} = \min_{\ell} \varepsilon_\ell, \tag{26}$$

is retained together with the harmonic order at which this minimum occurs. Table V summarizes the proximity measures for all 16 measurement records.

The proximity patterns vary substantially across the 16 records. Five records exhibit no collision within the specified guard ($\rho_{\mathrm{col}} = 0\%$), three exhibit partial collision occupancy, and eight exhibit persistent proximity, with an examined respiratory harmonic lying within the guard in every slow-time analysis window ($\rho_{\mathrm{col}} = 100\%$).

The cardiac errors further illustrate the relationship between harmonic proximity and estimation error. Four of the five records with cardiac errors greater than $5$ BPM are Records 02, 04, 05, and 07, all of which have $\rho_{\mathrm{col}} = 100\%$. However, persistent proximity does not always lead to a large error: Records 10–13 also have $\rho_{\mathrm{col}} = 100\%$ but cardiac errors no greater than $5$ BPM. Record 06 shows the opposite case, with a cardiac error greater than $5$ BPM and $\rho_{\mathrm{col}} = 0\%$. Thus,




(a) (b)

Fig. 11. Proximity of the Prony candidate to the examined respiratory harmonics for (a) Record 01 and (b) Record 02. The gray band denotes the $\pm 0.08$ Hz frequency guard around the Prony candidate. The star marks $\varepsilon_{\min}$, and red markers indicate collision windows.

proximity to a respiratory harmonic is an important ambiguity in the measurements, but it does not by itself explain the cardiac error in every record.

Fig. 11 shows how the proximity between the Prony candidate and the respiratory harmonics changes over time for Records 01 and 02. In Record 01, none of the examined respiratory harmonics enters the $\pm\varepsilon_0$ guard around the Prony candidate, resulting in $\rho_{\mathrm{col}} = 0\%$. In Record 02, the fourth harmonic (H4) trajectory remains within the guard in every slow-time analysis window, leading to $\rho_{\mathrm{col}} = 100\%$.

The geometric measures show when the Prony candidate approaches a respiratory harmonic, but not whether separate spectral components remain visible as their frequencies approach each other. We examine this question in the records with partial collision occupancy using time–frequency analysis.

Concentration of Frequency and Time (ConceFT) was introduced for time–frequency analysis of noisy multicomponent signals with time-varying amplitudes and instantaneous frequencies [25], and has been applied to physiological signals, including heart rate variability (HRV) and QT variability from ECG recordings [26], [27]. The complex quasi-uniform (CQU) variant, CQU-ConceFT, replaces the random projections of ConceFT with deterministic complex spherical designs [28], and has been demonstrated on physiological data for the analysis of time-varying spindle structure in N2-stage electroencephalogram (EEG) recordings [28].

In this work, CQU-ConceFT is used only as a diagnostic for the partial-collision records. It examines whether separate spectral components remain visible before and/or after the collision and how their time–frequency structure changes as the respiratory harmonic approaches the Prony candidate. This evidence supplements the geometric proximity analysis.

For the radar measurements, CQU-ConceFT is applied to the same phase observation obtained after PCA fusion in the baseline cardiac processing. The fixed H1–H5 respiratory harmonic notch filters are omitted so that the harmonic structure remains present in the observation. The signal is restricted to the $0.8$–$2.5$ Hz cardiac frequency range before the time–frequency analysis. CQU-ConceFT is implemented following the formulation of Sourisseau *et al.* [28]; implementation details are provided in that reference.

Record 03 provides a representative example of partial

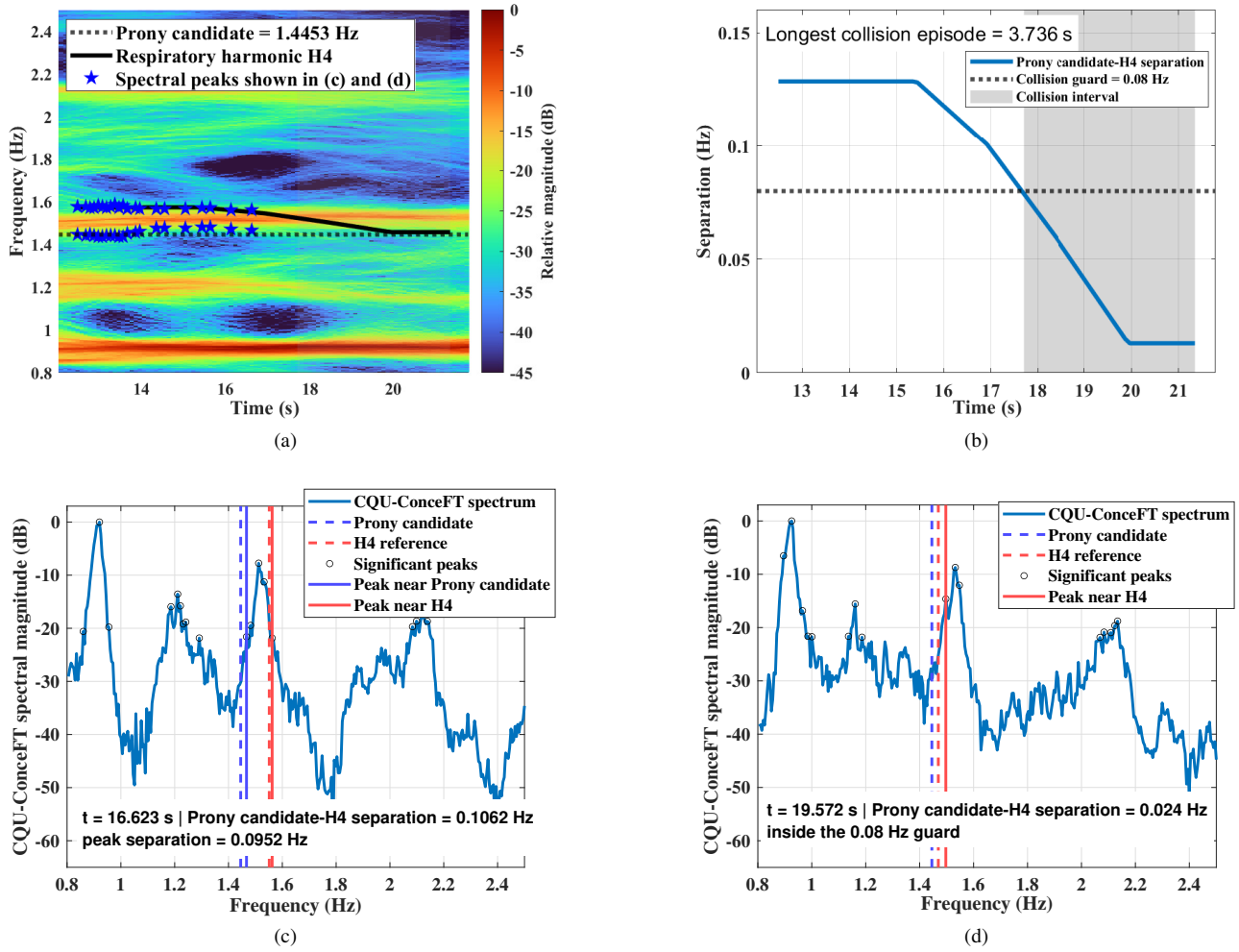



Fig. 12. Time–frequency and geometric analysis for Record 03: (a) CQU-ConceFT time-frequency representation, (b) candidate–H4 geometry relative to the 0.08 Hz collision guard, (c) spectrum before the collision, and (d) spectrum during the collision.

collision, with $\rho_{\mathrm{col}} = 42.857\%$ and H4 as the respiratory harmonic associated with the minimum separation. The CQU-ConceFT representation for this record is shown in Fig. 12a. Before the collision, at $t = 16.623$ s, the separation between the Prony candidate and H4 is $0.1062$ Hz, as shown in Fig. 12b. At the same time, the spectrum in Fig. 12c shows two nearby spectral peaks at approximately $1.4670$ and $1.5622$ Hz, corresponding to a separation of $0.0952$ Hz. The two spectral structures are therefore distinguishable before the collision, consistent with the geometric separation outside the collision guard.

Later, at $t = 19.572$ s, the candidate–H4 separation decreases to $0.0239$ Hz, placing the two frequencies within the $0.08$ Hz collision guard, as shown in Fig. 12b. The corresponding spectrum during the collision is shown in Fig. 12d. Thus, up to the onset of the collision, separate spectral components remain distinguishable in the time–frequency representation, and the geometric criterion does not indicate candidate–harmonic ambiguity. Once H4 enters the collision region, the geometric criterion identifies candidate–harmonic ambiguity.

Records 03, 08, and 14 are the three records with partial collision occupancy. In all three records, separate spectral components are visible outside the collision region, while the corresponding record-level cardiac estimates remain within $5$ BPM of the ECG references. These observations illustrate both the record-level agreement with ECG in the three partial-collision cases and the time-varying respiratory-harmonic ambiguity captured by the geometric criterion.

## VI. Conclusion

This work presented, to the best of our knowledge, the first experimental demonstration of contactless vital-sign sensing in the FR3 band. This demonstration was enabled by VitalFR3, a programmable FMCW measurement platform that integrates direct sampling with an Ettus USRP X440 and a SignalCraft SC2470 FR3 upconverter. The results showed that the complete transmit-receive chain should be treated as a single measurement instrument and characterized in amplitude, phase, and timing before physiological signal processing. Once this measurement reference is established, the calibrated complex I/Q measurements can be used for fast-time localization of a

persistent target response and to extract the respiratory and cardiac motion across multiple FR3 center frequencies.

Our measurements and processing algorithms demonstrated excellent agreement with the reference respiratory rates, while the fine cardiac estimation was more challenging in some measurements due to the dominance of the respiratory signal. An apnea measurement study provided additional evidence that cardiac-related motion could be better recovered when respiratory motion was reduced. Under normal breathing, however, the measurements revealed that respiratory harmonics can enter the cardiac frequency range, making frequency alone insufficient to determine the physiological origin of a component. Future work should extend the validation to more subjects and measurement conditions, and investigate methods that use additional signal information to distinguish cardiac motion from respiratory harmonics when their frequencies approach or overlap.

## ACKNOWLEDGMENT

The authors would like to thank N. Pandeya and M. Dickens of Ettus Research for their technical guidance and support in configuring the USRP X440 testbed; the SignalCraft Technologies team, particularly T. Wilson, for technical support related to the SC2470 FR3 up/down converter; and M. Majidimosleh of the iRadio Lab, University of Calgary, for discussions and technical advice on RF aspects of the experimental setup.

## REFERENCES

[1] G. A. Baduge, M. Vaezi, J. K. Dassanayake, M. Z. Hameed, E. Ollila, and S. A. Vorobyov, "Frequency Range 3 for ISAC in 6G: Potentials and Challenges," *IEEE Commun. Mag.*, vol. 64, no. 10, pp. 150–156, 2026.

[2] J. Pegoraro, G. Ventura, D. Tagliaferri, A. Bedin, M. Rossi, M. Mezzavilla, and J. Widmer, "Toward Multiband Sensing in FR3: Frequency Anisotropy Characterization and Non-Contiguous Bands Aggregation Algorithms," *npj Wirel. Technol.*, vol. 2, no. 1, p. 47, 2026.

[3] A. Bazzi, F. Gast, F. Liu, S. Jin, G. Fettweis, and M. Chafii, "From Coverage to Sensing: ISAC Meets FR3," *IEEE Commun. Mag.*, pp. 1–7, 2026.

[4] G. Bakhshi, M. A. Rawahi, N. Akhshatayeva, M. E. Hassan, M. Elsayed, Y. Elshenawy, S. D. Naicker, and H. Abou-Zeid, "RespiSense: Real-Time Respiration Monitoring Using a Low-Complexity WiFi SDR Platform," in *Proc. IEEE Global Commun. Conf. (GLOBECOM)*, 2025, pp. 973–979.

[5] D. Shakya, M. Ying, T. S. Rappaport, H. Poddar, P. Ma, Y. Wang, and I. Al-Wazani, "Comprehensive FR1(C) and FR3 Lower and Upper Mid-Band Propagation and Material Penetration Loss Measurements and Channel Models in Indoor Environment for 5G and 6G," *IEEE Open J. Commun. Soc.*, vol. 5, pp. 5192–5218, 2024.

[6] M. Ying, D. Shakya, T. S. Rappaport, P. Ma, Y. Wang, I. Al-Wazani, Y. Wu, and H. Poddar, "Upper Mid-Band Channel Measurements and Characterization at 6.75 GHz FR1(C) and 16.95 GHz FR3 in an Indoor Factory Scenario," in *Proc. IEEE Int. Conf. Commun. (ICC)*, 2025, pp. 1–6.

[7] D. Shakya, M. Ying, T. S. Rappaport, H. Poddar, P. Ma, Y. Wang, and I. Al-Wazani, "Propagation Measurements and Channel Models in Indoor Environment at 6.75 GHz FR1(C) and 16.95 GHz FR3 Upper-Mid Band Spectrum for 5G and 6G," in *Proc. IEEE Global Commun. Conf. (GLOBECOM)*, Dec. 2024, pp. 998–1003.

[8] K. F. Nieman, O. Kanhere, R.-K. Shiu, W.-J. Xu, C.-Y. Duan, and S. S. Ghassemzadeh, "An Adaptive cmWave/FR3 Channel Sounder for Integrated Sensing and Communication," in *Proc. IEEE Global Commun. Conf. (GLOBECOM)*, 2025, pp. 2886–2891.

[9] R. Bomfin, A. Rasteh, A. Bazzi, H. Guo, H. Lee, M. Mezzavilla, S. Rangan, J. Choi, and M. Chafii, "Multi-Band Channel Sensing in the Upper Mid-Band (FR3)," in *Proc. IEEE Global Commun. Conf. (GLOBECOM)*, 2025, pp. 5127–5132.

[10] M. Engelhardt, S. Giehl, M. Schubert, A. Ihlow, C. Schneider, A. Ebert, M. Landmann, G. del Galdo, and C. Andrich, "Accelerating Innovation in 6G Research: Real-Time Capable SDR System Architecture for Rapid Prototyping," *IEEE Access*, vol. 12, pp. 118 718–118 732, 2024.

[11] A. T. Kristensen, S. Li, A. Balatsoukas-Stimming, and A. Burg, "Monostatic Multi-Target Wi-Fi-Based Breathing Rate Sensing Using OpenWiFi," in *Proc. IEEE Wireless Commun. Netw. Conf. (WCNC)*, 2024, pp. 1–6.

[12] M. HosseinpourNiari and Z. G. Kashani, "Axial Ratio Alignment: A Critical Factor for Polarization Purity and Accuracy in 24 GHz Circularly-Polarized Doppler Radar for Vital Sign Monitoring," *IEEE Trans. Instrum. Meas.*, vol. 75, 2026.

[13] Y. Hu, Z. Xia, and F. Xu, "Investigating Respiration-Heartbeat Separation Through a Multipoint Scattering Chest Wall Motion Model: 60-GHz FMCW Radar Assessment," *IEEE Trans. Instrum. Meas.*, vol. 73, pp. 1–13, 2024.

[14] H. Zhu, Y. Zhao, Z. Zhang, H. Yi, C. Gao, F. Liang, C. Xu, J. Wang, and F. Qi, "Multidimensional Physiology-Inspired Enhanced Vital Sign Monitoring Using MIMO mmWave Bio-Radar," *IEEE Trans. Instrum. Meas.*, vol. 75, pp. 1–17, 2026.

[15] X. Qiao, Y. Su, X. Li, and T. Shan, "Millimeter-Wave Radar Vital Signs Measurement With Random Body Movement Using Missing Data Model," *IEEE Trans. Instrum. Meas.*, vol. 74, pp. 1–14, 2025.

[16] D. Xu, W. Yu, Y. Wang, and M. Chen, "Vital Signs Detection in the Presence of Nonperiodic Body Movements," *IEEE Trans. Instrum. Meas.*, vol. 73, pp. 1–16, 2024.

[17] Z. Liu, Y. Ye, D. Jiang, and S. Tu, "Robust Vital Signs Monitoring of Speaking Subjects Through mmWave Radar," *IEEE Trans. Instrum. Meas.*, vol. 74, pp. 1–15, 2025.

[18] F. Aghaei, M. Monemi, M. Rasti, and M. Uysal, "FR3 for 6G Networks: A Comparative Study Against FR1 and FR2 Across Diverse Environments," in *Proc. Joint Eur. Conf. Netw. Commun. & 6G Summit (EuCNC/6G Summit)*, 2026, pp. 960–967.

[19] F. Aghaei, M. Monemi, M. Rasti, and M. Uysal, "Characterization of FR3 Cellular Vehicle-to-Base Station Links in HighRise Urban Scenarios," in *Proc. IEEE Int. Conf. Commun. (ICC)*, 2026, pp. 1–6.

[20] H. Xu, J. Zhang, P. Tang, H. Xing, H. Miao, N. Zhang, J. Li, J. Wu, W. Yang, Z. Zhang, W. Jiang, Z. He, A. Haghighat, Q. Wang, and G. Liu, "Near-Field Propagation and Spatial Non-Stationarity Channel Model for 6–24 GHz (FR3) Extremely Large-Scale MIMO: Adopted by 3GPP for 6G," *IEEE J. Sel. Areas Commun.*, vol. 44, pp. 3201–3218, 2026.

[21] S. Shankar, R. K. Ganti, and J. K. Milleth, "FR3 OFDM Multistatic ISAC Geometry-Aware Multi-Link Fusion and CRLB-Guided Design," *IEEE Open J. Commun. Soc.*, vol. 7, pp. 6047–6065, 2026.

[22] D. Jiang, S. Tu, Y. Ye, and Z. Liu, "Virtual Radar Model and Processing for All-Directional Measurements of Vital Signs," *IEEE Trans. Instrum. Meas.*, vol. 74, pp. 1–14, 2025.

[23] C. Li, J. Ling, J. Li, and J. Lin, "Accurate Doppler Radar Noncontact Vital Sign Detection Using the RELAX Algorithm," *IEEE Trans. Instrum. Meas.*, vol. 59, no. 3, pp. 687–695, 2010.

[24] W. Liu, Y. Hu, Y. Chu, Y. Yang, S.-Y. Cao, Q. He, X. Zhang, and H.-L. Shen, "Remote Heart Rate Measurement Using UWB Radar via Multistage Adaptive Estimation," *IEEE Trans. Instrum. Meas.*, vol. 74, pp. 1–13, 2025.

[25] I. Daubechies, Y. G. Wang, and H.-t. Wu, "ConceFT: Concentration of Frequency and Time via a Multitapered Synchrosqueezed Transform," *Philos. Trans. R. Soc. A*, vol. 374, no. 2065, p. 20150193, 2016.

[26] Y.-T. Lin and H.-T. Wu, "ConceFT for Time-Varying Heart Rate Variability Analysis as a Measure of Noxious Stimulation During General Anesthesia," *IEEE Trans. Biomed. Eng.*, vol. 64, no. 1, pp. 145–154, 2017.

[27] H.-T. Wu and E. Z. Soliman, "A New Approach for Analysis of Heart Rate Variability and QT Variability in Long-Term ECG Recording," *Biomed. Eng. Online*, vol. 17, no. 1, p. 54, 2018.

[28] M. Sourisseau, Y. G. Wang, R. S. Womersley, H.-T. Wu, and W.-H. Yu, "Improve Concentration of Frequency and Time (ConceFT) by Novel Complex Spherical Designs," *Appl. Comput. Harmon. Anal.*, vol. 54, pp. 137–144, 2021.